Spin-wave switching using a dynamic magnonic crystal

Masashi Iwaba[1] and Koji Sekiguchi[2]*

[1]*Graduate School of Engineering Science, Yokohama National University, Tokiwadai 79-5, Yokohama 240-8501, Japan*
[2]*Faculty of Engineering, Yokohama National University, Tokiwadai 79-5, Yokohama 240-8501, Japan*

In this study, switching of the spin-wave propagation was investigated using an yttrium iron garnet (YIG) waveguide. A dynamic magnonic crystal was designed to control the non-reciprocal surface spin waves. The dynamic magnonic crystal controlled the periodic modulation field on the YIG film and caused a strong Bragg reflection on the surface spin waves. The maximum effect of Bragg reflection was analyzed by the wavelet to be 95% of its intensity. The spin-wave switching by the dynamic magnonic crystal will be a promising method of carrier-flow control for constructing the integrated magnonic circuits.

The application of magnonic devices to signal processing in magnonic integrated circuits has garnered significant research interest.[1,2] The magnon is the quantum of a spin wave and their flow, *i.e.*, the flow of the spin-angular momenta can be a new class of information carrier, without generating any Joule heat. These spin waves, comprising magnons, can flow even through insulators, unlike the electron current. Information processing devices such as the magnon transistors[3,4] and ψ-shaped spin-wave interferometers[5,6] have been developed using yttrium iron garnet (YIG) films. For example, a magnon transistor was designed using the source (excitation) and drain (detection) antennas; to control the magnon propagation, a gate antenna between the source and drain antennas was installed in combination with a magnonic crystal—comprising periodic stripe grooves[7–11] on the YIG film surface. The magnonic crystal was designed to enhance the nonlinear magnon-magnon interaction. In a more coherent magnon system, such as the spin wave, it is possible to control the spin-wave propagation using a periodic magnetic field as the spin waves encounter a strong Bragg reflection owing to the oscillating magnetic field.[12–14] Furthermore, the magnonic crystals which experience the influence of a magnetic field are known as dynamic magnonic crystals (DMCs).[15–18]

The evaluation of spin-wave attenuation by the DMC using the magnetostatic backward volume spin waves (MSBVWs) has been previously reported.[19–21] Recently, A. B. Ustinov *et.al.*[22] observed the spin-wave attenuation by an electric-field DMC using magnetostatic surface spin waves (MSSWs). However, the switching control of MSSWs has not yet been achieved as the carrier signal propagation. There is the essential problem that spin waves acquire a finite frequency bandwidth (Δf_{sw}) during the propagation in a dispersive medium. For instance, the bandwidth of MSSWs in Ustinov's pioneering report was Δf_{sw}=120 MHz, while the 5 dB attenuation band width was only Δf_{att}=1.5 MHz. Approximately 98% of total power of MSSW packet was unchanged. For the development of magnonic devices, a switching control over the MSSWs is essential because the MSSW mode provides a key feature of nonreciprocity,[23–25] which is the basic principle guiding the logic devices. The switching of MSSWs will serve the same crucial role as the gate control in the electronic CMOS devices.

In this study, the switching control over the propagation of the surface spin-wave was demonstrated using the rejection band of a double dynamic magnonic crystal. The real-time waveform and wavelet analysis reveal the switching behavior as well as the propagation of the MSSWs.

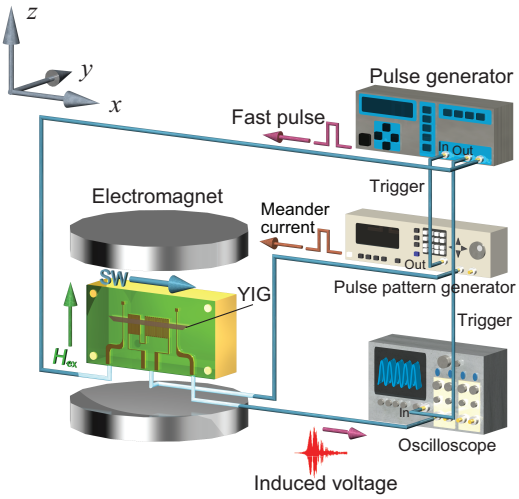

Fig. 1. (Color online) Schematic of the time-resolved measurements of spin-wave packet control. The transmission of a spin-wave packet is initiated and observed using a pair of excitation and detection antennas. The spin wave propagating through a YIG waveguide was controlled using a dynamic magnonic crystal placed between the antennas. The pulse generator, pulse pattern generator, and oscilloscope were synchronized by the trigger signals.

Time-resolved spin-wave spectroscopy was performed for the YIG waveguide, as represented in Fig. 1. The spin-wave waveguide is a YIG film epitaxially grown on a gadolinium gallium garnet (GGG).[26] The width and thickness of the YIG were 1.3 mm and 5 μm, respectively. Both edges of the waveguide were cut at an angle of 45° to prevent spin-wave reflection at the edge (Fig. 3(a)). The spin-wave packet was excited by introducing a fast pulse into a Cu antenna with a width of 75 μm (details of the antenna geometry are discussed later in Fig.3(a)). The amplitude, duration, and rise time of the microwave pulse were 4.7 V, 10 ns, and 65 ps, respectively, at a frequency of 100 kHz. An external magnetic field (H_{ex}) was applied in the z direction, normal to the propagation direction (x) to ensure the propagation of the spin waves in the MSSW mode. The spin wave signal was detected in the form of an induced voltage by the detection antenna connected to the 20

*Corresponding author: sekiguchi-koji-gb@ynu.ac.jp

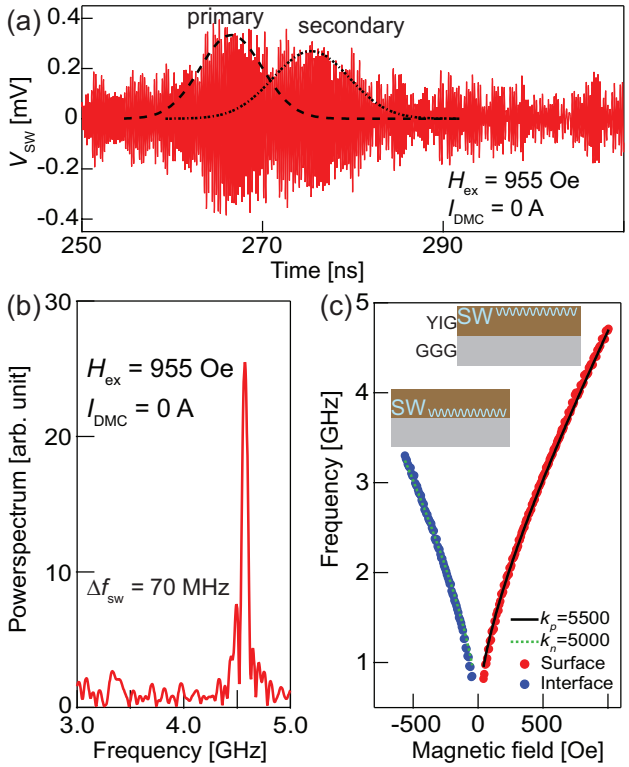

Fig. 2. (Color online) (a) Real-time waveform of the spin wave in the YIG waveguide and (b) power spectrum of the waveform calculated using fast Fourier transform (FFT) analysis. The magnetic field was H_{ex} = 955 Oe. (c) Magnetic field dependence of the center of resonant frequency the spin waves. The $f - H$ relations were fitted using the MSSW dispersion relations.

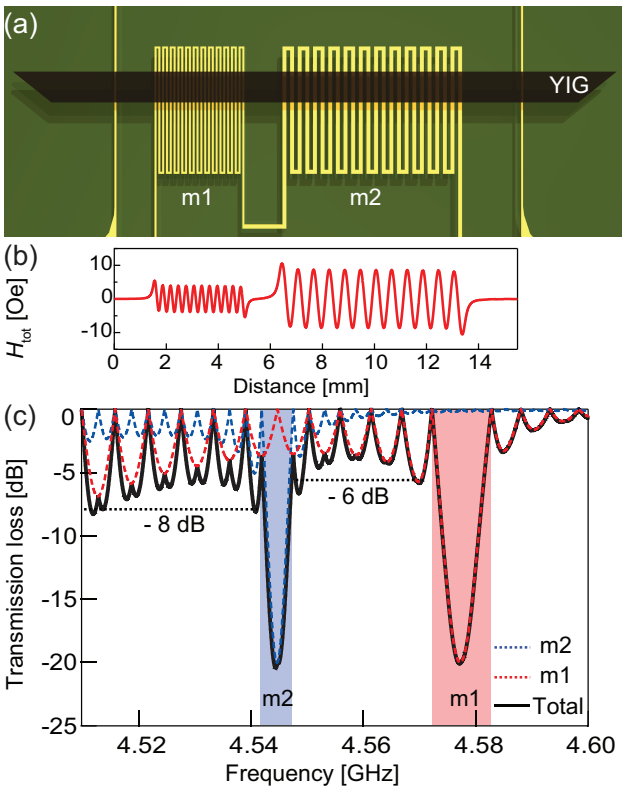

Fig. 3. (Color online) (a) Detailed illustration of the excitation and detection antennas and the double magnonic crystal comprising of the meander structure m1 and m2. (b) Magnetic field profile generated by a double magnonic crystal. (c) Calculated transmission loss (rejection band) of a double magnonic crystal after application of an external magnetic field H_{ex} = 955 Oe. The red dashed line represents the transmission loss of meander m1, and the blue dashed line represents the transmission loss of meander m2. The solid black line represents the total transmission loss.

GHz sampling oscilloscope (DCA-J 86100C). The distance between the excitation and detection antennas was 15.5 mm.

Figure 2(a) represents a real-time waveform of the spin waves in the absence of a magnonic crystal, and controlled with an applied magnetic field of H_{ex} = 955 Oe in the z direction. The real-time waveform comprises two independent packets with a separation time of 10 ns. The packet labeled by the primary packet originates from the leading edge of the excitation pulse, whereas the packet labeled by the secondary packet originates from the falling edge. The time separation was changed by altering the duration of the fast excitation pulse. The resonant frequency was calculated using FFT and shown in Fig. 2(b). The center of the resonant frequency is 4.57 GHz and exhibits a frequency dispersion Δf_{sw}= 70 MHz. The magnetic field dependence of the resonant frequency is shown in Fig. 2(c). Using the theoretical dispersion relation,[24)]

$$f = \frac{\gamma}{2\pi}\sqrt{\left(H_{ex} + \frac{4\pi M_s}{2}\right)^2 - \left(\frac{4\pi M_s}{2}\right)^2 e^{-2kd}} \qquad (1)$$

where the gyromagnetic ratio is γ = 17.6 MHz/Oe, and the YIG film thickness is d = 5.1 μm, The propagation mode of the spin wave was confirmed to be the MSSW mode. The deduced wavenumbers were k_p = 5500 ± 320 rad/m for magnetic fields with positive values and k_n = 5000 ± 450 rad/m for a magnetic field with negative values. The saturation magnetization was $4\pi M_s$ = 1750 G, which agrees to the previous report.[21)]

Since the nonreciprocity of the MSSW mode in a positive magnetic field forces the spin-wave to localize at the top side of the YIG film, a positive-valued magnetic field was applied for the spin-wave switching experiment, as shown in the inset of Fig. 2(c). The spin waves arrive close to the detection antenna and dynamic magnonic crystal. The lack of data points for the negative-valued magnetic fields indicates that the spin waves propagate far from the antennas and the signal has been diminished.

To conduct the spin-wave switching experiment, a double DMC placed underneath the YIG waveguide was utilized (see Fig. 3(a)).

The double DMC and the Cu antennas were fabricated on another FR4 substrate, and the YIG waveguide prepared on the GGG substrate was placed upside down on the antennas. The advantage of double DMC structure is that the rejection bandwidth can be extended to cover entire spin-wave frequency Δf_{sw}= 70 MHz. The single meander DMC[16)] and single stipe[15)] could not cover the Δf_{sw}= 70 MHz, because the attenuation bandwidth was narrower than Δf_{att}=30 MHz and resulted in 20~30% attenuation of total spin-wave power. The insufficient attenuations can not apply to the switching control of MSSWs, because the 70~80% power of MSSW packet can be delivered by the carrier frequencies within Δf_{sw}= 70 MHz.

The DMC comprises different meander structures named m1 and m2 with different stripe spacings; these structures

generate local magnetic fields[16)]

$$H_{\mathrm{m1}}(x) = \sum_{1\le j\le 2n}^{n} (-1)^j H_{\mathrm{stripe}}(x-(j-1/2-n)g), \quad (2)$$

$$H_{\mathrm{m2}}(x) = \sum_{1\le j\le 2n} (-1)^j H_{\mathrm{stripe}}(x-(j-1/2-n)g), \quad (3)$$

$$H_{\mathrm{stripe}}(x) = \frac{I_{\mathrm{DMC}}}{5}\left[\tan^{-1}\left(\frac{x-x'}{s}\right)\right]_{x'=-g/2}^{x'=+g/2}, \quad (4)$$

where the parameter s = 100 μm is the distance between the meander and YIG surface, the integer n = 15 is the number of stripes, the parameter g is gap between the meander lines, and the integer j is the index number ranging from 1 to $2n$. I_{DMC} denotes the current.

The x component of the periodic magnetic fields $H_{\mathrm{tot}}(x) = H_{\mathrm{m1}}(x) + H_{\mathrm{m2}}(x)$ act as a source of Bragg reflection against the spin waves owing to the direct torque on the magnetization. The intensity of the Bragg reflection increases if the spatial period of the meander matches the spin-wave wavelength λ. The wavenumber $k = 2\pi/\lambda$ dependence of the Bragg reflection can be estimated by calculating the Fourier components $F(k)$ of $H_{\mathrm{tot}}(x)$. $F(k)$ is given by,[16)]

$$F(k) = i\frac{4\pi I_{\mathrm{DMC}}}{5}\frac{e^{-|ks|}}{|k|}\sin\left(\frac{kl}{2}\right)\sum_{j=1}^{n}(-1)^{j+1}\sin\left[(2j-1)kl\right] \quad (5)$$

where k is the wavenumber, and l is the width of the meander stripe. $F(k)$ only provides a structural scattering factor (k dependence of spin-wave scattering); however, it is possible to estimate a rejection band structure because the wavevector k corresponds to the carrier frequency f via the MSSW dispersion relation.

To control the propagation of the spin-wave packet shown in Fig. 2(a), the line widths of the DMC were set as l_{m1} = 75 μm and l_{m2} = 150 μm. The DMCs can apply a modulation magnetic field H_{m1} = 4.12 Oe and H_{m2} = 8.86 Oe on the YIG surface, and manipulate the non-reciprocal spin wave localized at the top side of the YIG. The spatial distribution of the modulation magnetic field is illustrated in Fig. 3(b). Because it is difficult to determine the absolute magnitude of the rejection strength, the rejection band i.e., the transmission loss was calculated by setting the maximum value to -20 dB, as shown in Fig. 3(c). The sharp dips at 4.58 GHz and 4.54 GHz correspond to the meander m1 and m2, respectively. Note that the designed rejection band was extended to 4.52 < f < 4.60 GHz (Δf_{att}= 80 MHz) owing to the superposition of two independent DMCs and covered the frequency dispersion Δf_{sw} of the spin-wave packet.

The spin-wave switching experiment was performed at H_{ex} = 955 Oe, as shown in Fig. 4. As shown in the bottom panel of Fig. 4(a), the spin-wave packet appears at 258 < t < 282 ns and shows a peak-to-peak voltage of 0.76 mV. To understand the time-frequency representation, the wavelet transform $w(1/\Delta t, t)$ of V_{sw} was calculated using the following formula:

$$w = \int_{-\infty}^{\infty} dx \frac{1}{\sqrt{|\Delta t|}}\psi\left(\frac{x-t}{\Delta t}\right)V_{\mathrm{sw}}(x) \quad (6)$$

where ψ is the wavelet mother function (Gabor function).[27,28)] The intensity of the spin wave was determined to be $W = |w|^2$

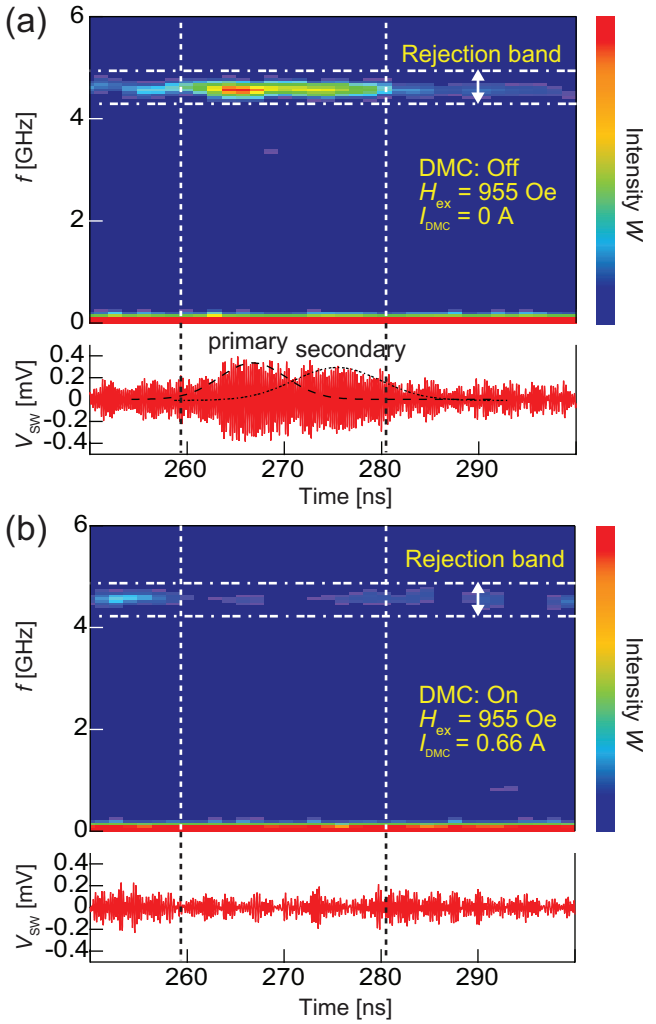

Fig. 4. (Color online) Spin-wave switching by the double magnonic crystal. (a) Wavelet transforms of the spin-wave packets without a control current I_{DMC} =0. The spin wave packet was located at 258 < t < 282 ns. The frequency dispersion is within the designed rejection band. (b) Wavelet transforms of the spin-wave packet when the control current I_{DMC} = 0.66 A was applied. The signals from the primary and secondary packets disappear.

around t with a frequency $f \sim 1/\Delta t$. As shown in the top panel of Fig. 4(a), the strong power of the spin wave is located at 265 ns, and the frequency distribution of the spin-wave packet is Δf_{sw} ~70 MHz. This packet is exactly within the range of the designed rejection band 4.52 < f < 4.60 GHz.

The DMC was then driven by a pulse current I_{DMC} =0.66 A, having t_d = 300 ns duration with 10 μs period. The duty ratio was 0.03. As shown in the bottom panel of Fig. 4(b), the spin-wave packets disappeared perfectly. The wavelet analysis also proved that the strongest intensity of the primary packet decreased by 95%. By accumulating the power P of primary and secondary packets using the formula:

$$P = \int_{4.52\mathrm{GHz}}^{4.60\mathrm{GHz}}\int_{258\mathrm{ns}}^{282\mathrm{ns}} W(t,f)dtdf, \quad (7)$$

The signal to noise ratio SNR (=20log[$P_{I_{\mathrm{DMC}}=\mathrm{off}}/P_{I_{\mathrm{DMC}}=\mathrm{on}}$]) was calculated to be 74% (12 dB). The frequency band was determined using the width of the rejection band 4.52 < f < 4.60 GHz. on/off switching of MSSW was achieved using the designed double-DMC.

Finally, we examined the current I_{DMC} and the duty-ratio

dependencies. Figure 5 shows the SNR dependence of I_{DMC}. Because the effects of current and duty ratio would induce the thermal effect, the on/off switching experiment (SNR) was averaged over 10 experiments for each current pulse. For the duty set at 0.03, as represented by the solid line in Fig. 5(a), the SNR shows a maximum value of 8 dB at 0.66 A. This reflects the fact that the modulation field becomes strong. In contrast, the decrease of SNR at 0.72 A suggests that the heating by double-DMC increases the thermal noise in real-time waveforms. A heating effect was clearly observed when the duty ratio increased as represented by the broken lines in Fig. 5(a). The SNR did not increase monotonically because the thermal noise in the real-time waveform increased in the spin-wave off state (thus, $P_{I_{DMC}=on}$) owing to a longer I_{DMC} pulse injection. For a larger duty ratio, the maximum SNR appears at lower current values, as indicated by the arrows in Fig. 5(a). The SNRs are all suppressed compared the case where the duty is set at 0.03, exhibiting the contribution of the heating effect as shown in Fig. 5(b).

The magnitude of control current (voltage) will be an open issue for realization of magnonic circuit. For the fast switching magnonic device such as magnonic transistor, the power consumption could be roughly evaluated by effective power $P_{eff} = V^2/2Z_0$ for characteristic impedance Z_0= 50 Ω. In case of double DMC, the control voltage for 74 % power-reduction corresponds to 33 V. The control voltage of electric field DMC was 1800 V for 2% power-attenuation.[22] The power consumption of double DMC is at least 1/3000 of electric field DMC. Furthermore, the control voltage of double DMC can be greatly reduced by using thinner YIG films, since the control voltage is determined by the strength of modulation field at the localization depth of MSSWs.

In this study, we demonstrated the on/off switching behavior of the magnetostatic surface wave packet. By designing the double magnonic crystal structure, the modulation magnetiield profile and rejection band profiles were estimated for the surface spin-wave packet. Furthermore, the wavelet analysis adequately demonstrated the on/off switching of the spin wave in the time and frequency domains. The SNR was evaluated by changing the control current. Considering the design of the magnonic crystal evaluated in this study, the optimized current and duty ratio were obtained as 0.66 A and 0.03, respectively. The spin-wave switching presented in this paper will serve as the basic technique of the magnonic signal processing devices.

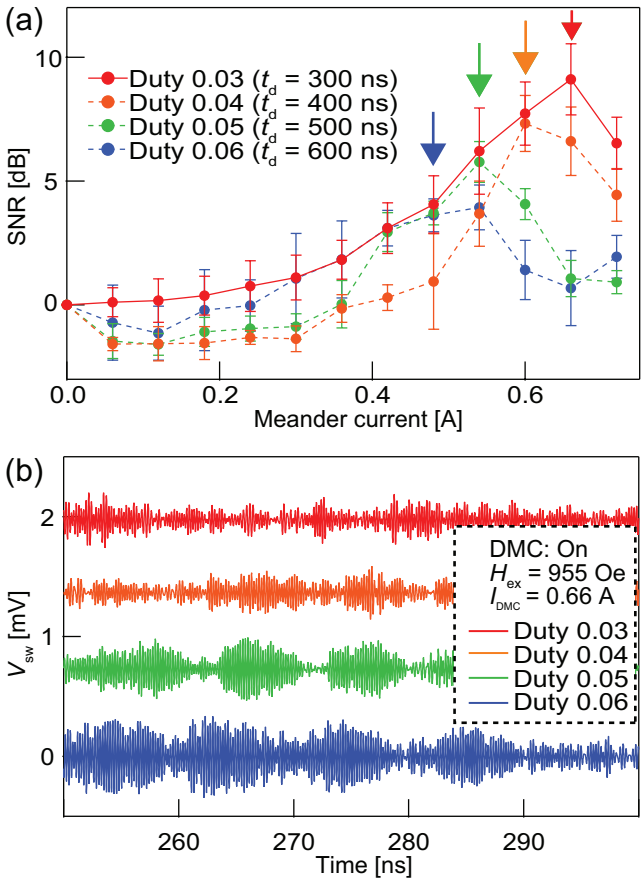

Fig. 5. (Color online) (a) Meander current I_{DMC} dependence of signal to noise ratio (SNR). The SNR at duty 0.03, shows a maximum at 0.66 A. The duty-ratio dependence shows a strong reduction in the SNR because of the heating effect. (b) Increase of thermal noise effect on the spin-wave off state.

Acknowledgments

This work was supported by the Grants-in-Aid for Scientific Research (19H00861 and 18H05346) from the Japan Society for the Promotion of Science (JSPS). This work was partly supported by the Grants-in-Aid for Scientific Research (20H05652).

1) A. Chumak, V. Vasyuchka, A. Serga, and B. Hillebrands, *Nat. Phys.* **11**, 453 (2015).
2) K. Sekiguchi, D. Chiba, and T. Tachizaki, *Jpn. J. Appl. Phys.* **57**, 0902B4 (2018).
3) A. Chumak, A. Serga, and B. Hillebrands, *Nat. Commun.* **5**, 4700 (2014).
4) K. Sekiguchi, *AAPPS Bulletin* **28**, 2 (2018).
5) N. Kanazawa, T. Goto, K. Sekiguchi, A. Granovsky, C. Ross, H. Takagi, Y. Nakamura, H. Uchida, and M. Inoue, *Sci. Rep.* **7** and 7898 (2017).
6) S. Klingler, P. Pirro, T. Brächer, B. Leven, B. Hillebrands, and A. Chumak, *Appl. Phys. Lett.* **105**, 152410 (2014).
7) T. Goto, K. Shimada, Y. Nakamura, H. Uchida, and M. Inoue, *Phys. Rev. Appl.* **11**, 014033 (2019).
8) K. Chi, Y. Zhu, R. Mao, S. Nikitov, Y. Gulyaev, and C. Tsai, *IEEE Trans. Magn.* **47** 3708 (2011).
9) A. Chumak, A. Serga, S. Wolff, B. Hillebrands, and M. Kostylev, *J. Appl. Phys.* **105**, 083906 (2009).
10) C. Romero, Z. Ortiz, A. Drozdovskii, B. Kalinikos, M. Huerta, J. Juárez, G. Maldonado, N. Qureshi, O. Kolokoltsev, and G. Monsivais, *J. Appl. Phys.* **120**, 043901 (2016).
11) H. Qin, G. Both, S. Hämäläisen, L. Yao, and S. Dijken, *Nat. Commun.* **9**, 5445 (2018).
12) M. Alam, Y. Liu, and D. Yue, *J. Fluid. Mech.* **624**, 191 (2009).
13) A. Chumak, P. Dhagat, D. Jander, A. Serga, and B. Hillebrands, *Phys. Rev. B* **81**, 140404(R) (2010).
14) R. Zivieri, S. Tacci, F. Montoncello, L. Giovannini, F. Nizzoli, M. Madami, G. Gubbiotti, G. Carlotti, S. Neusser, G. Duerr, and D. Grundler, *Phys. Rev. B* **85**, 012403 (2012).
15) T. Neumann, A. Serga, B. Hillebrands, and M. Kostylev, *Appl. Phys. Lett.* **94**, 042503 (2009).
16) A. Chumak, T. Neumann, A. Serga, B. Hillebrands, and M. Kostylev, *J. Phys. D: Appl. Phys* **42**, 205005 (2009).
17) A. Chumak, V. Tiberkevich, A. Karenowska, A. Serga, J. Gregg, A. Slavin, and B. Hillebrands, *Nat. Commun* **1**, 141 (2010).
18) A. Karenowska, J. Gregg, V. Tiberkevich, A. Slavin, A. Chumak, A. Serga, and B. Hillebrands, *Phys. Rev. Lett.* **108**, 015505 (2012).
19) N. Sato, S. Lee, K. Lee, and K. Sekiguchi, *J. Phys. D Appl. Phys.* **50**, 094004 (2017).
20) M. Kawase, M. Iwaba, K. Sekiguchi, *Jpn. J. Appl. Phys.* **59**, SEED01 (2020).
21) M. Iwaba, S. Fujiwara, and K. Sekiguchi, *T. Magn. Soc. Special Issues*

(Jpn) **4**, 18-22 (2020)
22) A. Ustinov, A. Drozdovskii, A. Nikitin, A. Semenov, D. Bozhko, A. Serga, B. Hillebrands, E. Lähderanta, and B. Kalinikos, *Commu. Phys.* **2**, 137 (2019).
23) K. Sekiguchi, S. Lee, H. Sukegawa, N. Sato, S. Oh, R. McMichael, and K. Lee, *NPG Asia Materials* **9**, e392 (2017).
24) K. Sekiguchi, K. Yamada, S. Seo, K. Lee, D. Chiba, and T. Ono, *Appl. Phys. Lett.* **97**, 022508 (2010).
25) T. Schneider, A. Serga, T. Neumann, B. Hillebrands, and M. Kostylev, *Phys. Rev. B* **77**, 214411 (2008).
26) The YIG film was grown by INNOVENT e.V. Technologieentwicklung Jena, Germany.
27) C. Chui, "An introduction to wavelets academic press", *New York* (1992).
28) K. Sekiguchi, A. Yamaguchi, H. Miyajima, and A. Hirohata, *Phys. Rev. B* **77**, 140401(R) (2008).